Inertial waves in a rotating spherical shell

By M. RIEUTORD[1,2] and L. VALDETTARO[3]

[1]Observatoire Midi-Pyrénées, 14 av. E. Belin, F-31400 Toulouse, France

[2]CERFACS, 42, Avenue Coriolis, F-31057 Toulouse, France

[3]Dipartimento di Matematica, Politecnico di Milano, Piazza L. da Vinci, 32, 20133 Milano, Italy

The structure and spectrum of inertial waves of an incompressible viscous fluid inside a spherical shell are investigated numerically. These modes appear to be strongly featured by a web of rays which reflect on the boundaries. Kinetic energy and dissipation are indeed concentrated on thin conical sheets, the meridional cross-section of which forms the web of rays. The thickness of the rays is in general independent of the Ekman number E but a few cases show a scaling with $E^{1/4}$ and statistical properties of eigenvalues indicate that high-wavenumber modes have rays of width $O(E^{1/3})$. Such scalings are typical of Stewartson shear layers. It is also shown that the web of rays depends on the Ekman number and shows bifurcations as this number is decreased.

This behaviour also implies that eigenvalues do not evolve smoothly with viscosity. We infer that only the statistical distribution of eigenvalues may follow some simple rules in the asymptotic limit of zero viscosity.

1. Introduction

The recent development of superconducting gravimeters has opened a new window on the liquid core of the Earth with the possibility of detecting small motions of this fluid with respect to the solid inner core or the solid outer mantle. Aldridge & Lumb (1987) were the first to propose that inertial waves could be detected in gravimetric data. For the moment, only the spinover mode of the liquid core has been detected (Neuberg, Hinderer & Zürn 1987) as it is associated to the nearly diurnal free wooble of the Earth. The detection of inertial modes, which are typical of rapidly rotating fluids, would be an opportunity to have access to physical properties of the liquid core of the Earth, like the viscosity or the stratification which are little known at present time (Lumb & Aldridge 1991). Inertial modes, which will be studied below, are also suspected to play some part in the geodynamo in particular because some of them are destabilized by the elliptic shape of the boundaries due to the tides (see Lumb, Aldridge & Henderson 1993; Kerswell 1994). While the Earth's core offers an almost canonical example for the studies of inertial modes in a spherical shell (the core's fluid, liquid iron, has a low viscosity and is weakly compressible, thus making the use of an incompressible fluid a good approximation), rapidly rotating stars are also places where these modes should be important, in particular because of the mixing they may induce; in this latter case however, inertial modes will also be coupled to gravity modes and density variations will be important.

Despite the fact that inertial modes have been known for a long time (Bryan 1889), their properties when the container is a spherical shell are rather ill-known. Bryan

solved the inviscid problem in the full sphere since separation of variables can be achieved in this case. In general, no such possibility exists for the shell and therefore solving the viscous problem with perturbation methods based on boundary layer theory is not possible.

In the inviscid limit inertial modes are governed by a hyperbolic equation (Poincaré equation for pressure). This is an additional difficulty since the problem is therefore mathematically ill-posed; however, one may use ray theory to study the propagation of characteristics and thus get informations about the solutions. This line of research led Stewartson to discover the probable pathological character of inviscid solutions in a spherical shell (see Stewartson & Rickard 1969; Stewartson 1971, 1972*a,b*). Such solutions are associated with a partly or wholly continuous spectrum. Those found by Stewartson (1972*a*) are low-frequency modes trapped in the equatorial region of a very thin shell. This is however a partial answer to the question of the nature of the spectrum of these modes in a shell when viscosity vanishes. For the full sphere, the spectrum is dense in $[0, 2\Omega]$ but discrete (Ω is the angular velocity of the sphere) and as viscosity decreases all eigenvalues converge smoothly to their asymptotic limit. For the shell, we shall see that this is certainly not the case.

As will be shown below, solutions can be very complex. Even if the problem is linear, a large range of scales is present in a single mode. The different scales which occur in a solution are related to the existence of many internal layers which are spawned by singularities of the boundary layers like the one arising at the critical latitude (see Kerswell 1995). These shear layers, which have been studied in the past by Stewartson (1957) and Walton (1975) on the simplified setup of coaxial rotating disks, have been reconsidered recently by Kerswell (1995) and Hollerbach & Kerswell (1995) in connection with the problem of precession of fluids. The main conclusion from these works is that despite the fact that these layers seem to play a minor role in the linear theory, they are important when nonlinear effects are considered.

This paper will present results obtained from a numerical resolution of the linearized viscous equations in spherical shells. Two shells have been considered: a thick one where the ratio of the inner to outer radius $\eta = 0.35$ is similar to that of Earth's liquid core, and a thin shell, $\eta = 0.80$, which can apply to Jupiter's deep atmosphere. Thanks to a powerful eigenvalue solver, we have been able to compute inertial modes at Ekman numbers as low as 10^{-9}. This low value is probably still too high for the Earth's core where current estimates give $E \sim 10^{-15}$ (Roberts 1988), but is relevant for Jupiter where estimations of the turbulent viscosity based on mixing-length theory lead to $E \sim 10^{-8}$.

The main result of the paper is that individual eigenmodes do not follow any precise asymptotic law as viscosity tends to zero; only statistical properties of these modes satisfy some simple rules (scalings). This problem is in fact related to another eigenvalue problem in physics, namely quantum chaos.

The paper has been organized as follows. In §2 we describe the method used for solving the equations of motion. In §3 we present our results and §4 draws some conclusions and presents future developments.

2. Formulation of the problem

2.1. *Equations*

Let R and ηR be the radii of the outer and inner shells ($\eta < 1$), Ω the angular velocity of the undisturbed fluid and ν the kinematic viscosity of the fluid. We shall

scale the perturbation equations using R as the length scale and $(2\Omega)^{-1}$ as the time scale.

As we are concerned only with infinitesimal perturbations, we discard nonlinear terms from the beginning. With the scales defined above, the dimensionless equations for the perturbations written in the frame rotating with constant angular velocity Ωe_z, are

$$\left.\begin{aligned} \lambda\boldsymbol{u} + \boldsymbol{e}_z \times \boldsymbol{u} &= -\nabla p + E\Delta\boldsymbol{u}, \\ \nabla \cdot \boldsymbol{u} &= 0. \end{aligned}\right\} \tag{2.1}$$

Here $\boldsymbol{u}$ is the velocity field of the perturbations and p is the reduced pressure perturbation. We introduced the Ekman number

$$E = \frac{\nu}{2\Omega R^2}.$$

As we are interested in the eigenmodes of the system, we assumed the perturbations to be proportional to $e^{\lambda t}$, with λ as the complex eigenvalue.

Equations (2.1) are completed with boundary conditions on the velocity; we take them to be no-slip ($\boldsymbol{u} = \boldsymbol{0}$) or stress-free ($\boldsymbol{e}_r \times \boldsymbol{\sigma}\boldsymbol{e}_r = \boldsymbol{0}$), where $\boldsymbol{\sigma}$ is the stress tensor and $\boldsymbol{e}_r$ is the unit radial vector.

2.2. *Numerical method*

The above equations define an eigenvalue problem which can be solved using spectral decomposition. The operator has a compact resolvent and therefore its spectrum consists of discrete eigenvalues of finite multiplicity (see Chossat 1979 and references therein).

Using spherical coordinates, we expand the fields in spherical harmonics for the angular part and in Chebyshev polynomials for the radial part. Therefore we first write

$$\boldsymbol{u} = \sum_{l=0}^{+\infty}\sum_{m=-l}^{+l} u_m^l(r)\boldsymbol{R}_l^m + v_m^l(r)\boldsymbol{S}_l^m + w_m^l(r)\boldsymbol{T}_l^m,$$

where

$$\boldsymbol{R}_l^m = Y_l^m(\theta,\phi)\boldsymbol{e}_r, \qquad \boldsymbol{S}_l^m = \nabla Y_l^m, \qquad \boldsymbol{T}_l^m = \nabla \times \boldsymbol{R}_l^m$$

and where $Y_l^m(\theta,\phi)$ are normalized spherical harmonics. Following some simple rules, given in Rieutord (1987), the equation of vorticity may be projected rather easily onto spherical harmonics. The radial parts then obey the following system:

$$\left.\begin{aligned} E\Delta_l w_m^l + \left(\frac{im}{l(l+1)} - \lambda\right)w_m^l \\ = -A(l,m)r^{l-1}\frac{\mathrm{d}}{\mathrm{d}r}\left(\frac{u_m^{l-1}}{r^{l-2}}\right) - A(l+1,m)r^{-l-2}\frac{\mathrm{d}}{\mathrm{d}r}\left(r^{l+3}u_m^{l+1}\right), \\ \\ E\Delta_l\Delta_l(ru_m^l) + \left(\frac{im}{l(l+1)} - \lambda\right)\Delta_l(ru_m^l) \\ = B(l,m)r^{l-1}\frac{\mathrm{d}}{\mathrm{d}r}\left(\frac{w_m^{l-1}}{r^{l-1}}\right) + B(l+1,m)r^{-l-2}\frac{\mathrm{d}}{\mathrm{d}r}\left(r^{l+2}w_m^{l+1}\right), \end{aligned}\right\} \tag{2.2}$$

where

$$A(l,m) = \frac{1}{l^2}\left(\frac{l^2 - m^2}{4l^2 - 1}\right)^{1/2}, \quad B(l,m) = l^2(l^2 - 1)A(l,m), \quad \Delta_l = \frac{1}{r}\frac{d^2}{dr^2}r - \frac{l(l+1)}{r^2}.$$

Boundary conditions on radial functions read

$$\left.\begin{array}{ll} u_m^l = v_m^l = w_m^l = 0, & \text{no slip,} \\\\ u_m^l = \dfrac{d^2 r u_m^l}{dr^2} = \dfrac{d}{dr}\left(\dfrac{w_m^l}{r}\right) = 0, & \text{stress free.} \end{array}\right\} \tag{2.3}$$

System (2.2) is an infinite set of differential equations where the coupling between radial functions of indices $l-1$, l and $l+1$ is due to Coriolis force. Note that different m are not coupled.

We have shown in Rieutord (1991) that analytical solutions exist for the truncated system. These solutions may be expressed in terms of Bessel functions and polynomials. They have been used for testing the accuracy of the development on the Chebyshev basis.

Let us rewrite (2.2) formally as

$$L_A X = \lambda L_B X,$$

where L_A and L_B are two complex linear differential operators and λ is the eigenvalue. X is an eigenvector like

$$X_{m^+}\begin{vmatrix} u_m^m(r) \\ w_m^{m+1}(r) \\ u_m^{m+2}(r) \\ \vdots \\ \vdots \end{vmatrix} \quad \text{or} \quad X_{m^-}\begin{vmatrix} w_m^m(r) \\ u_m^{m+1}(r) \\ w_m^{m+2}(r) \\ \vdots \\ \vdots \end{vmatrix}$$

if the solution is symmetric (X_{m^+}) or antisymmetric (X_{m^-}) with respect to the equatorial plane.

Now each radial function is approximated by a truncated expansion of $N+1$ Chebyshev polynomials. Thus each of these functions may be represented either by its spectral components or by its values on the Gauss–Lobatto collocation nodes. We shall use the latter representation. In such case, differential operators d^k/dr^k are represented by full matrices of size $(N+1)$. As the system (2.2) couples radial functions of indices $l-1$, l and $l+1$, it will yield a tridiagonal block matrix.

To take into account the boundary conditions, we write the final system in the following form:

$$\begin{pmatrix} \boldsymbol{A}_{NL}^m & \boldsymbol{C}_{NL}^T \\ \boldsymbol{C}_{NL} & 0 \end{pmatrix}\begin{pmatrix} u_{NL}^m \\ \epsilon_{NL}^m \end{pmatrix} = \lambda \begin{pmatrix} \boldsymbol{B}_{NL}^m & 0 \\ 0 & 0 \end{pmatrix}\begin{pmatrix} u_{NL}^m \\ \epsilon_{NL}^m \end{pmatrix}. \tag{2.4}$$

Here $\boldsymbol{A}_{NL}^m$ and $\boldsymbol{B}_{NL}^m$ are square matrices of order $(L-m+1)(N+1)$, arising from the expansion into spherical harmonics up to order L and the discretization of the differential equations on the $N+1$ collocation nodes; $\boldsymbol{C}_{NL}$ is the $3(L-m+1)$ by $(L-m+1)(N+1)$ matrix corresponding to the discretization of the boundary conditions on the two boundaries and $\boldsymbol{C}_{NL}^T$ is the transpose of $\boldsymbol{C}_{NL}$. The ϵ_{NL}^m are $3(L-m+1)$ auxiliary variables which, in the limit of large N, should tend to zero
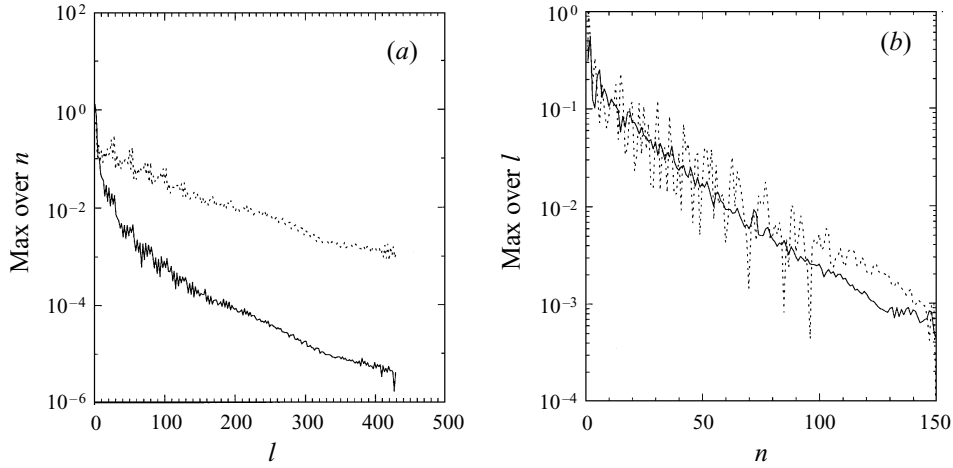
FIGURE 1. Spectra of the spherical harmonic components (*a*) and the Chebyshev coefficients (*b*). In the spherical harmonic spectrum, we have separated the poloidal field (u_l^m dotted line) and the torodial field (w_l^m solid line). For each *l* or *n* (the spherical harmonic and Chebyshev indices respectively), the maximum value over the other spectral component is always chosen. The spectra are for the $I_{\eta=0.35}$ mode with $E = 10^{-8}$.

(Fox & Parker 1968; Orszag 1971). They are therefore an indication of the precision of the approximation.

The complex generalized eigenvalue problem (2.4) may be solved using either a 'direct' method or an iterative one. The direct method is based on the QZ algorithm, which yields the whole spectrum of eigenvalues and, if required, the whole set of eigenfunctions. This method for solving linear eigenvalue problems has been extensively used in literature (see e.g. Orszag 1971; Gottlieb & Orszag 1977). It provides a very fast convergence to the true eigenmodes when the resolution is increased. However attention must be paid to spurious eigenvalues which might also appear (see Gardner, Trogden & Douglas 1989; McFadden, Murray & Boisvert 1990). The spurious eigenvalues are distinguished by the fact that if the resolution is increased they do not converge to any precise value. In practice we perform two different computations at two different resolutions and we discard the eigenvalues that have substantially changed. Actually, in our computations we never observed the occurrence of spurious eigenvalues in the part of the spectrum with the least-damped modes.

The iterative method is based on the incomplete Arnoldi–Chebyshev method (Braconnier, Chatelin & Dunyach 1995). A shift-and-invert strategy has been implemented. Instead of solving $\boldsymbol{A}\boldsymbol{x} = \lambda \boldsymbol{B}\boldsymbol{x}$, the code solves the eigenproblem $\boldsymbol{B}\boldsymbol{x} = \mu(\boldsymbol{A} - s\boldsymbol{B})\boldsymbol{x}$ and the desired eigenvalues are $\lambda = s + 1/\mu$. This strategy gives access to eigenvalues close to the shift *s*. In particular by choosing $s = i\omega$ ($i^2 = -1$ and $\omega \in \mathbb{R}$) we obtain the least-damped eigenmodes with frequency close to ω.

The direct method has the advantage of giving the whole spectrum of eigenvalues/eigenvectors. However the memory and time requirements become prohibitive when resolution is increased since the sparsity of the matrices $\boldsymbol{A}$ and $\boldsymbol{B}$ is not preserved by the QZ algorithm. Therefore a total of $[(L - m + 1)(N + 4)]^2$ elements must be stored for both matrices. The algorithm is also highly time consuming: the number of floating-point operations for the algorithm is between $[(L - m + 1)(N + 4)]^3$ and $[(L - m + 1)(N + 4)]^4$.
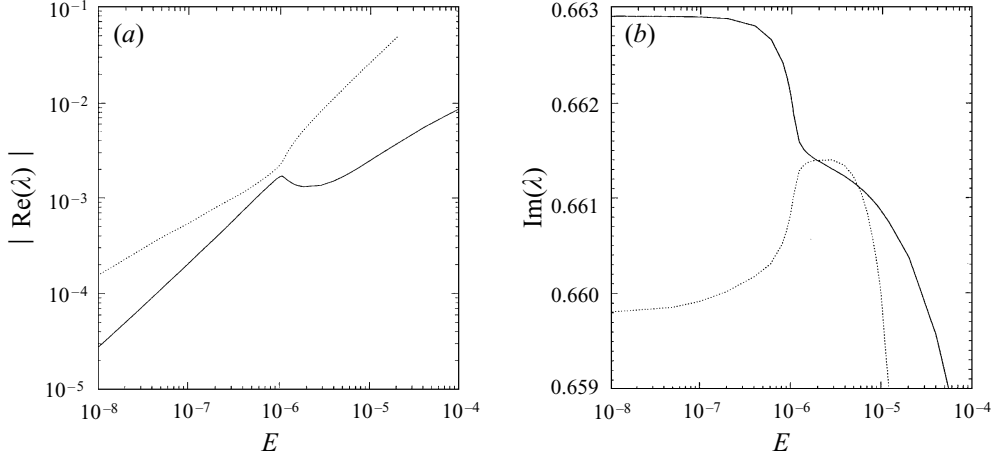
FIGURE 2. Scaling laws of the damping rate (*a*) and frequency (*b*) of the two eigenvalues plotted on figure 3. The dotted line is for the mode $I_{\eta=0.35}$ while the solid line refers to the mode $II_{\eta=0.35}$.

The iterative method instead preserves the sparsity of the matrices, and therefore the memory requirement drops to order $27(L - m + 1)(N + 1)^2/2$. This method can also be used to follow particular eigenvalues down to very low Ekman numbers, or to produce the least-damped part of the spectrum (by varying $s = i\omega$ from $\omega = -1$ to 1).

Finally, we display in figure 1 some spectral components of a solution computed at high resolution ($L = 430$ and $N = 150$), for a low value of the Ekman number (10^{-8}). These spectra show the spectral convergence of the solution. The precision of the computation can also be controlled *a posteriori* by inspection of the resulting eigenfunctions: from figure 7 for example, we see that the smallest structures, i.e. shear layers, are well resolved.

3. Results

3.1. *The mode structure*

To display the structure of the modes we have chosen to plot the kinetic energy and the viscous dissipation in a meridional plane. The first quantity reveals the amplitude of the velocity field of the mode while the second emphasizes the internal shear layers. Their expressions are

$$E_k = \tfrac{1}{2}u^2, \qquad \mathscr{D} = \tfrac{1}{2}E\left(s_{rr}^2 + s_{\theta\theta}^2 + s_{\phi\phi}^2 + 2(s_{r\theta}^2 + s_{r\phi}^2 + s_{\theta\phi}^2)\right)$$

where s_{ij} are the components of the rate-of-strain tensor in spherical coordinates.

In all cases presented here we have computed the modes using stress-free boundary conditions, except for the spin-over mode (figure 12*a*); this allowed us to show more clearly internal shear layers otherwise strongly dominated by Ekman layers.

As clearly shown by the different plots of figures 4, 5, 6, 8*a* and 9*a*, inertial modes in a spherical shell are featured by the characteristics of the Poincaré equation if the Ekman number is low enough. We might therefore expect that this structure results from an inviscid balance of forces. Hence, the structure of the modes should be independent of boundary conditions and persist asymptotically when the Ekman number tends to zero.
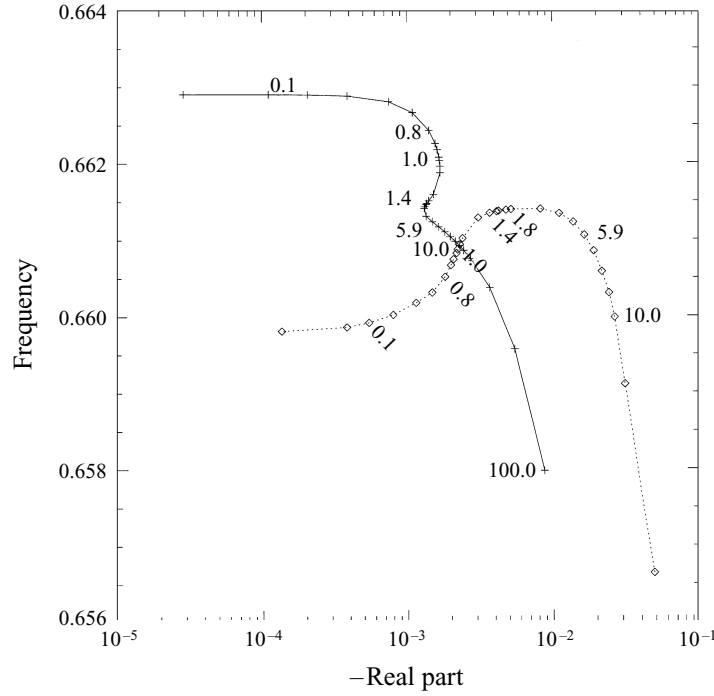
FIGURE 3. Path of the eigenvalues in the complex plane. The numbers inside the graph correspond to $10^6 E$.

The first point seems to be verified: in the few cases where we have computed the solutions for both no-slip and stress-free boundary conditions, the kinetic energy was distributed in the same way. Because of Ekman layers, this was not the case for dissipation.

The second point is surprisingly not true: the patterns of the modes change as the Ekman number is decreased.

The first mode we have been investigating in a detailed manner is an axisymmetric one which corresponds to the (4,1,0) mode of the full sphere in Greenspan notation with frequency $\omega/2\Omega = \sqrt{3/7} = 0.6547$ (Greenspan 1969). This mode is the least-damped one of the full sphere in the 0^+ symmetry. (We use the notation m$^\pm$ for modes having an $\exp im\phi$ dependence, and being symmetric (+) or antisymmetric (−) with respect to the equator.) Following this mode as the Ekman number was decreased, we noticed that the damping rate was increasing for E between 10^{-6} and 1.4×10^{-6} (figure 2a). A close look at this strange behaviour showed us that another mode was getting close to it in the complex plane, as clearly shown on figure 3. In fact the two modes exchange around $E = 10^{-6}$ as shown in the plots of the eigenfunctions at various Ekman numbers (figures 4 and 5). We shall denote these two modes I$_{\eta=0.35}$ and II$_{\eta=0.35}$ hereafter. (We note however that the two eigenvalues can never be confused: they remain distinct for each Ekman number.) A first consequence of such mode-crossing is that it is difficult, if not impossible, to anticipate the shape of a mode at very low Ekman numbers given a numerical solution at some moderately low Ekman number (e.g. 10^{-6}).

This raises the question of the existence of solutions in the asymptotic limit $E = 0$

$E = 5.0 \times 10^{-8}$

$E = 1.0 \times 10^{-7}$

$E = 4.0 \times 10^{-7}$

$E = 8.0 \times 10^{-7}$
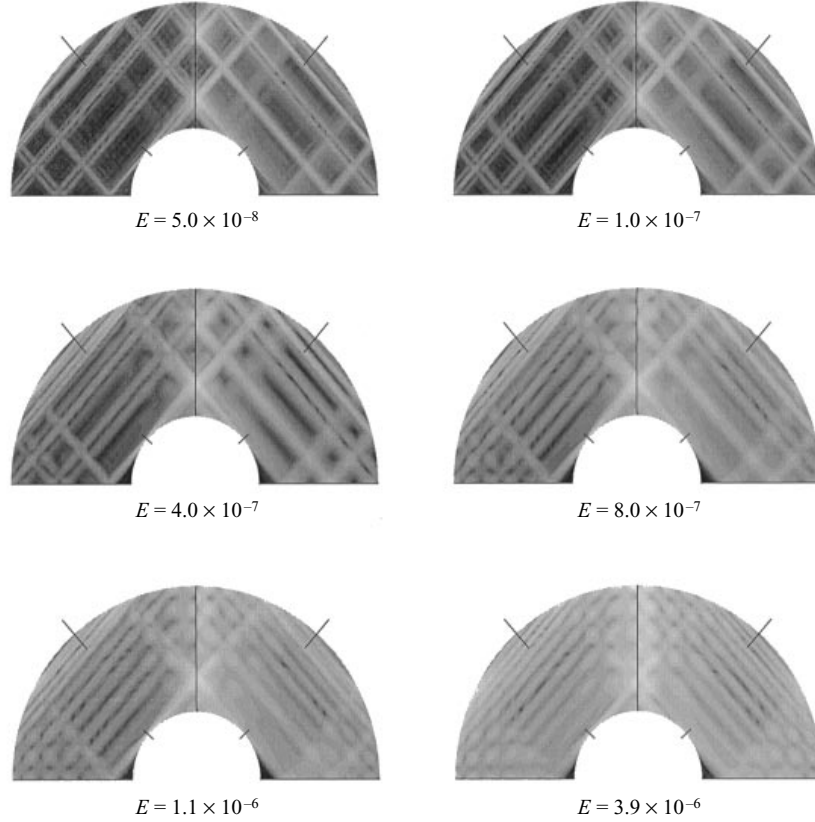
$E = 1.1 \times 10^{-6}$

$E = 3.9 \times 10^{-6}$

FIGURE 4. Structure of the mode $I_{\eta=0.35}$ (dotted line on figures 2 and 3) as a function of the Ekman number.

for inertial modes in a spherical shell. We shall try to give some evidence that no asymptotic solution should be expected in the general case.

3.2. *The ray pattern*

If one is concerned with the inviscid limit, the ray pattern is the feature to be investigated. Rays are indeed the signature of the hyperbolic nature of the inviscid equations.

We recall that for plane inertial waves energy propagates perpendicularly to the phase; therefore in a local analysis, the ray (which is in fact the meridian section of a cone) is an equiphase surface on which energy is 'flowing'. If s is the radial distance to the rotation axis, it may be shown (see Appendix A) that kinetic energy diverges as $1/s$ along the characteristics. This is the reason why modes are always 'brighter' close to the rotation axis (figure 6). As illustrated on figure 7 and shown in Appendix A, the velocity is parallel to the ray. In figure 7(*b*) we also clearly see that there is a strong shear in the meridional velocity in the direction perpendicular to the ray. We note that this strong shear is well captured by the numerical grid, each thin ray having at least 10 grid points in the transversal direction. We finally note that rays emerging almost radially have small amplitudes because the associated group velocity is small and the corresponding wavenumber is large implying a strong damping of the ray (see figure 6*a* or 9).
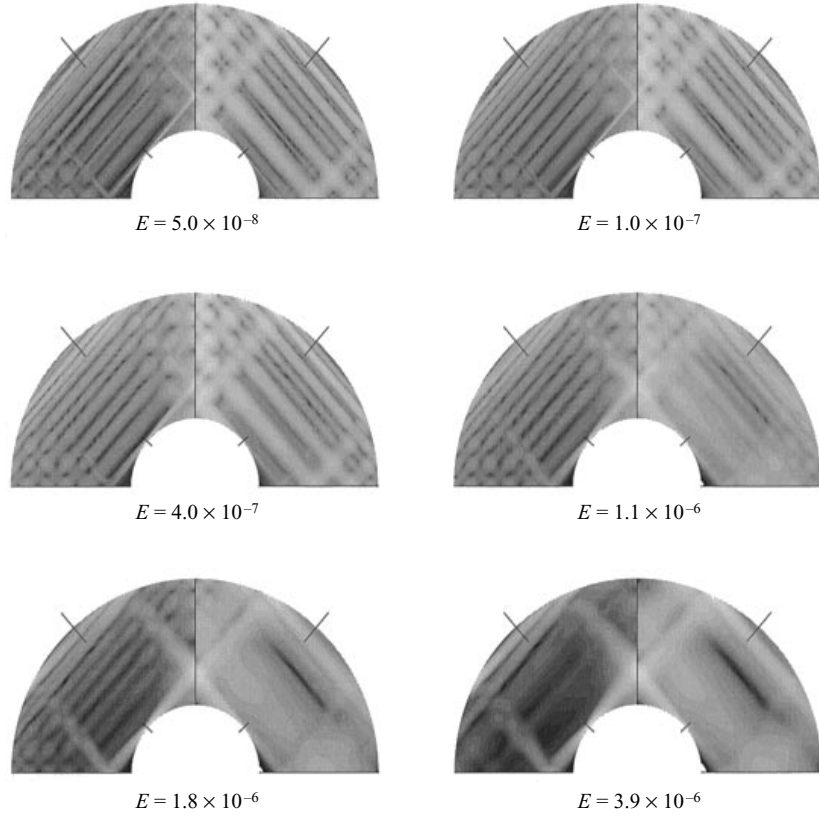
FIGURE 5. Structure of the mode $II_{\eta=0.35}$ (solid line on figures 2 and 3) as a function of the Ekman number. Kinetic energy is on the right quadrant of each plot while dissipation is on the left one. Tickmarks on the inner sphere indicate the critical latitude while those on the outer sphere indicate the direction of characteristics.

As already mentioned in the introduction, the first detailed examinations of the ray structure were given by Stewartson (1971, 1972*a*, *b*) and Israeli (1972). Stewartson has used a closed ray pattern to find the shape of trapped modes in the equatorial region of very thin shells. In such case, the closed ray pattern seems to define a region of space where the stream function may not vanish. In the inviscid limit, this function has an amplitude and a spatial frequency which tends to infinity as the limit cycle is approached. It may be interesting to see if such a behaviour shows up in our solutions.

For this purpose, we considered a mode of our thin shell for which the kinetic energy displayed a closed ray pattern (figure 8*a*). We shall label this mode $I_{\eta=0.80}$. Using the laws of reflection of inertial waves (Greenspan 1969), it is not difficult to compute quasi-analytically a ray pattern which has the same topology and show that it is indeed a limit cycle for ray propagation (see figure 8*b*; dark patterns of figure 8*b* match light patterns of figure 8*a*). As for trapped modes computed by Stewartson, this closed ray pattern exists only in a narrow range of frequencies:

$$0.7544 < \omega < 0.7550. \tag{3.1}$$

However, this is rather far from the observed frequency 0.743 and the difference

(a)

$\omega = 0.6598, \tau = -1.6 \times 10^{-4}$

(b)

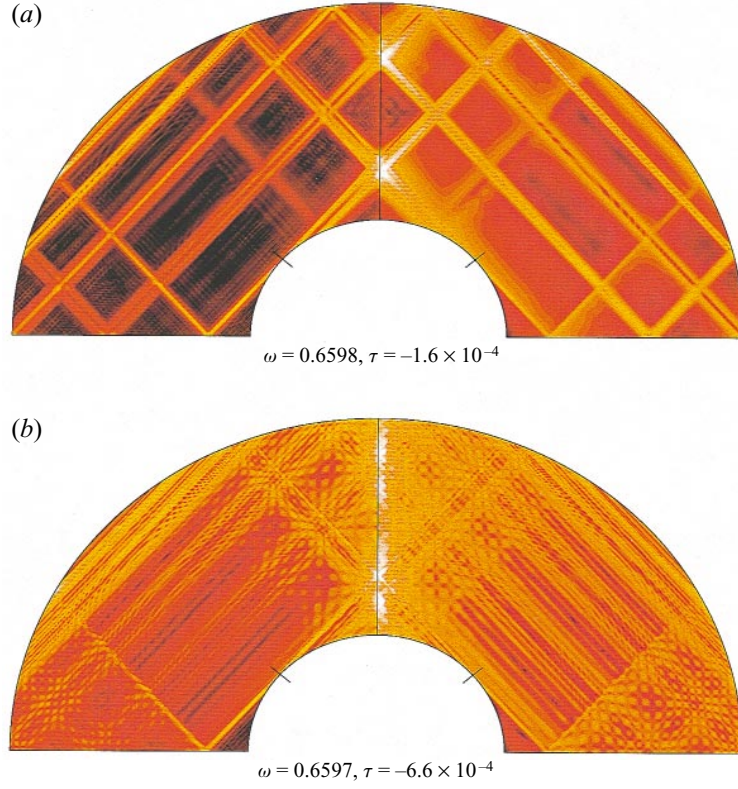$\omega = 0.6597, \tau = -6.6 \times 10^{-4}$

FIGURE 6. Two axisymmetric inertial modes with $\omega \approx 0.660$. The Ekman number is $E = 10^{-8}$ and the resolution is $L = 430$ and $N = 150$. Note the difference in ray trajectories: the first mode concentrates its energy in a small fraction of space defined by a periodic orbit of rays while the second mode displays an almost space-filling web of rays which imposes high spatial frequencies and a more efficient damping.
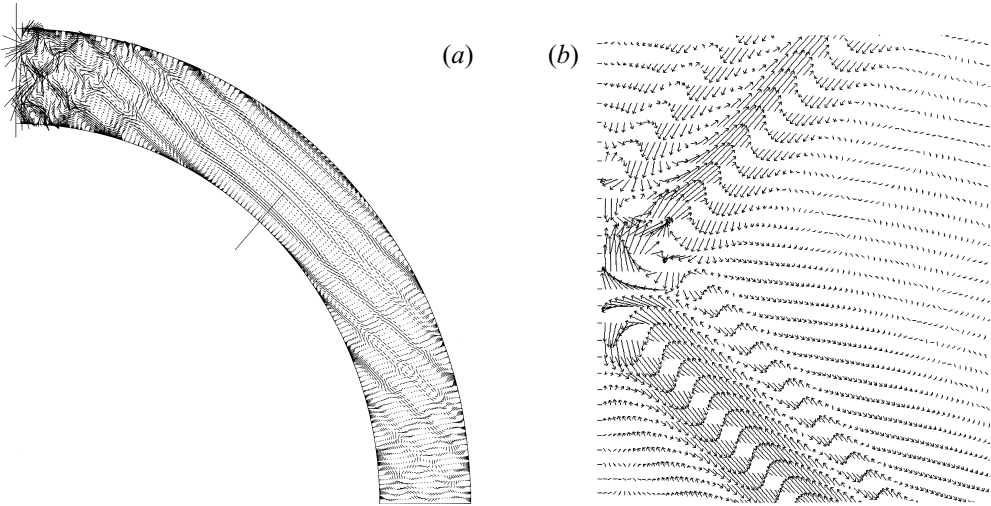

(a)   (b)

FIGURE 7. The velocity field in the (r, θ)-plane. (a) The mode $\text{II}_{\eta=0.80}$ and $E = 10^{-9}$. (b) magnification near the intersection of two rays for the mode $\text{I}_{\eta=0.35}$ and $E = 10^{-8}$. Note that in both cases the velocity is almost parallel to the ray propagation.
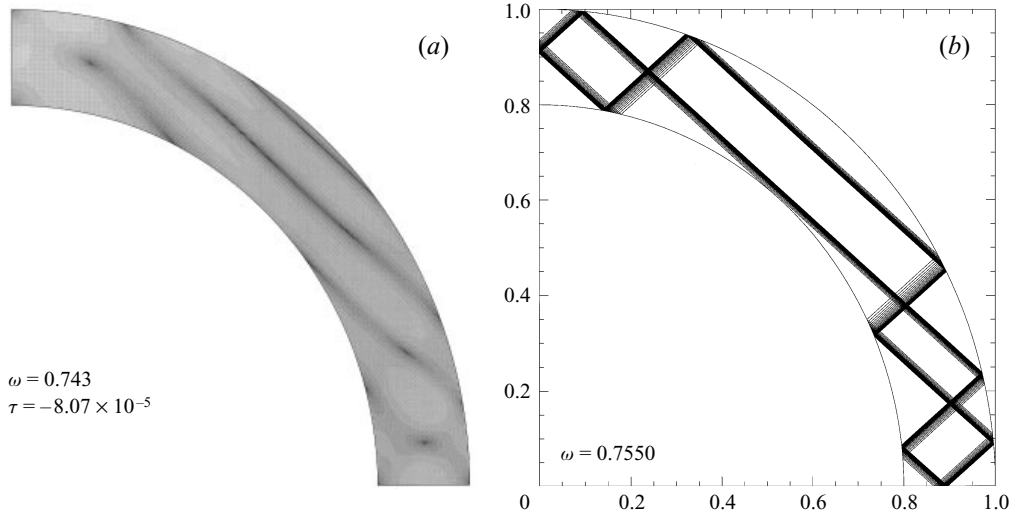
FIGURE 8. Kinetic energy of a large-scale mode (labelled $I_{\eta=0.80}$) for the thin shell (*a*) and ray pattern that matches the maxima of kinetic energy (*b*). Note that this pattern was found for a slightly different frequency (see also text and figure 9).
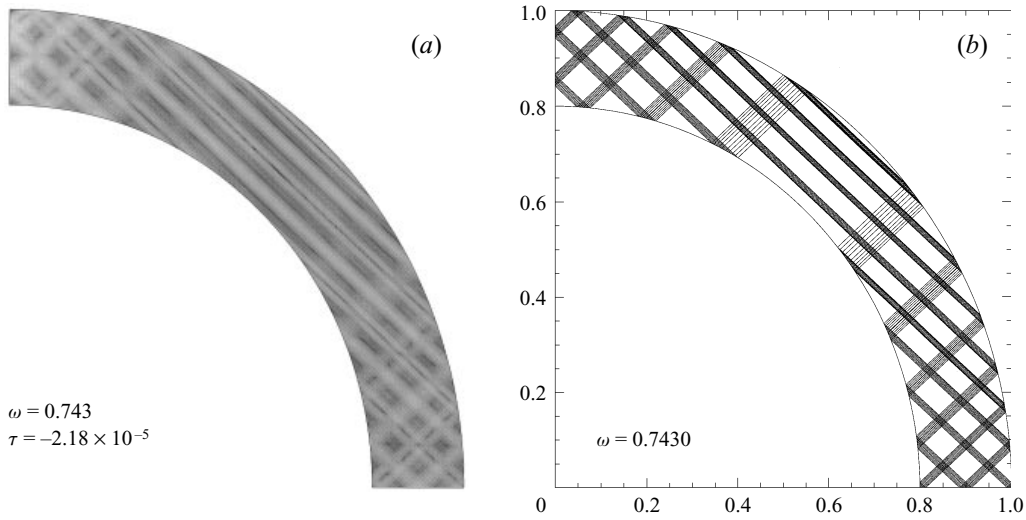

FIGURE 9. Kinetic energy (*a*) and the corresponding ray-pattern (*b*) for the mode $II_{\eta=0.80}$ when $\eta = 0.80$ and $E = 10^{-9}$.

cannot be attributed to viscous effects since variations of Ekman number induce $O(E)$ variations in frequency. Rather, this difference should be explained by the fact that ray theory is not quite appropriate for such modes because energy is not concentrated in a thin layer around the ray.

Despite the discrepancy in frequencies, the similarity between the observed mode and the limit cycle lets us think that we have got here an almost inviscid solution which should remain as $E \rightarrow 0$. This is not quite the case: the above-mentioned limit cycle is not 'structurally stable', to keep with the language of dynamical sys-

tems. At lower E (below 10^{-8}), a new structure appears which is closer to the ray pattern obtained for a frequency of 0.743 (see figure 9). We shall label this mode $II_{\eta=0.80}$

However the structure of the mode is still rather smooth and does not show the rapid oscillations predicted by Stewartson. The reason is that such modes (with rapid oscillations) are more strongly damped and therefore cannot be found among the least-damped modes. Since the mode which has the limit cycle displayed on figure 8(*b*) was not found at $E = 10^{-9}$, we explored the modes around $\omega = 0.755$ at this same Ekman number; we found there a mode with a large damping rate (50 times higher than the mode $I_{\eta=0.35}$) displaying strong oscillations very similar to the second mode of figure 6 which may be reminiscent of the behaviour mentioned by Stewartson.

Finally let us come back to the structural stability of the modes and the existence of asymptotic solutions. The mode $I_{\eta=0.80}$ as featured by the ray pattern of figure 8(*b*) only exists in the range $10^{-8} \lesssim E \lesssim 10^{-4}$. At lower Ekman numbers we have seen that it is replaced by a more complex pattern. We can already say that the structural stability of this new pattern will be weaker in the following sense: the number of reflection points is indeed far greater than for the previous pattern. If one of the points is moved by some small amount, then each point is moved by an amount increasing with its distance (i.e. the number of reflections) from the displaced point; therefore the range of frequencies where the cycle exists narrows as the number of reflection points increases. This result has been exemplified by Stewartson (1972*a*) in the case of trapped modes.

From these observations, two scenarios are possible:

 (i) At some very low Ekman number, variations of frequency due to viscosity are too small to destabilize the mode and therefore an asymptotic solution exists. This is the case of modes described in Appendix B.

(ii) The range of frequencies in which a closed ray pattern exists decreases faster than the viscous dependence of frequencies. (This range of frequencies is actually difficult to estimate and the interval given by (3.1), which was computed using ray trajectories, is certainly too large.) The mode keeps changing as the Ekman number decreases, developing still higher spatial frequencies, and no asymptotic solution exists. The damping rate, then, does not decrease as a power-law of the Ekman number.

3.3. *Rays and shear layers*

Patterns that appear in the numerical solutions may be reminiscent of shear layers and therefore it is interesting to see how their width scales with viscosity. We have found four cases.

The first case consists of patterns whose width is almost independent of viscosity. This was observed for instance in the modes $II_{\eta=0.35}$ of the thick shell and $I_{\eta=0.80}$ of the thin shell. In figure 10(*a*) we illustrate such a behaviour. The real part of the eigenvalue then decreases as E.

In the second case, the width of the rays constituting the pattern has a scaling consistent with $E^{1/4}$. We have observed this behaviour on the $I_{\eta=0.35}$ mode as shown by figure 10(*b*). In this case, the kinetic energy as well as the dissipation is concentrated in thin layers. Assuming that the main contribution to the total kinetic energy (E_k) and dissipation (D) is from these rays, one can easily estimate the damping rate:
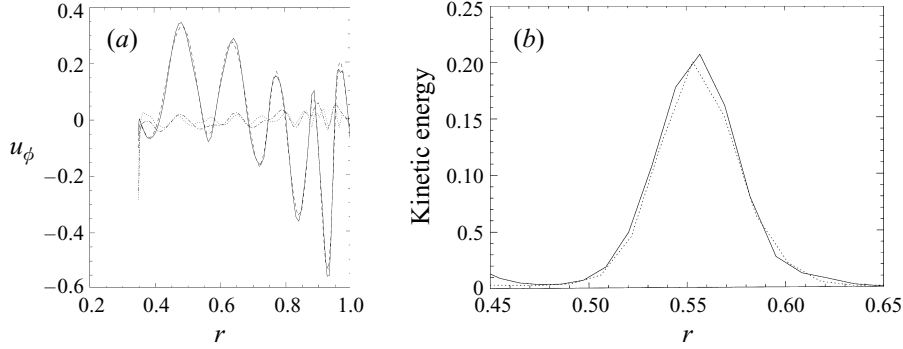
FIGURE 10. (a) Profiles of the ϕ-component of the velocity in the radial direction at critical latitude for the mode $\mathrm{II}_{\eta=0.35}$. The solid and dashed lines represent the real part of u_ϕ for $E = 5 \times 10^{-8}$ and $E = 2 \times 10^{-7}$ respectively. The dotted and dash-dotted correspond to the imaginary part. (b) Profiles of the kinetic energy in the radial direction at critical latitude for the mode $\mathrm{I}_{\eta=0.35}$. The solid line is for $E = 4 \times 10^{-7}$, the dashed line for $E = 10^{-8}$. The horizontal scale for the $E = 10^{-8}$ curve has been magnified by the factor $(4 \times 10^{-7}/10^{-8})^{1/4}$.
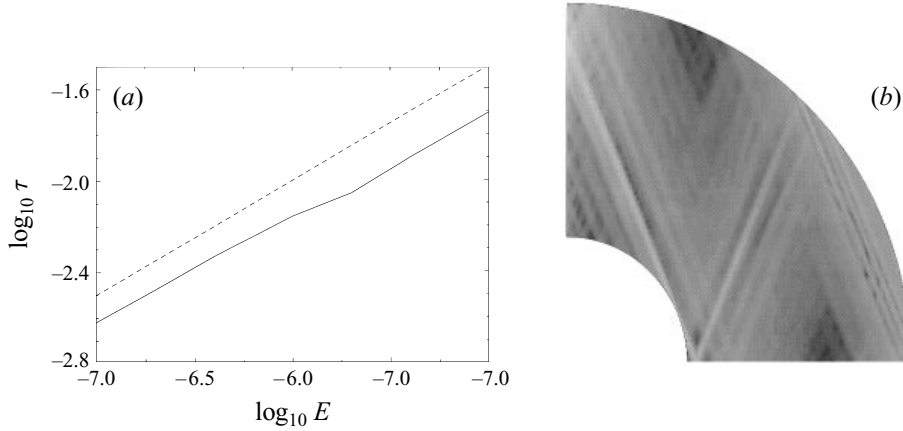

FIGURE 11. (a) The $\log_{10}$ of the damping rate for the least-damped mode having $\mathrm{Im}(\lambda) \sim 0.386$ is plotted versus the $\log_{10}$ of the Ekman number (solid line). The dashed line corresponds to the law $\tau \sim E^{1/2}$. (b) Kinetic energy of the mode for $E = 2 \times 10^{-7}$.

$\partial/\partial x$ scales like $E^{-1/4}$ and the volume of the rays is proportional to their width $E^{1/4}$; therefore

$$|\lambda_R| = \frac{D}{2E_k} \sim E \frac{\int_V \left(\frac{\partial u}{\partial x}\right)^2 \mathrm{d}^3 x}{\int_V u^2 \mathrm{d}^3 x} \sim E^{1/2}.$$

This value is quite compatible with the observed behaviour (see table 1 or figure 2).

The scaling $|\lambda_R| \sim E^{1/2}$ has been observed on several other modes. We give another example in figure 11 for a mode of the thick shell with $\mathrm{Im}(\lambda) \sim 0.4$. Note that between $E = 10^{-6}$ and $E = 10^{-5.6}$ the mode undergoes a transition, which produces a local change of the scaling from the $E^{1/2}$ law.

The third case corresponds to Stewartson layers of width $O(E^{1/3})$. These shear layers which result from a balance of inertia, Coriolis force and viscous force (see
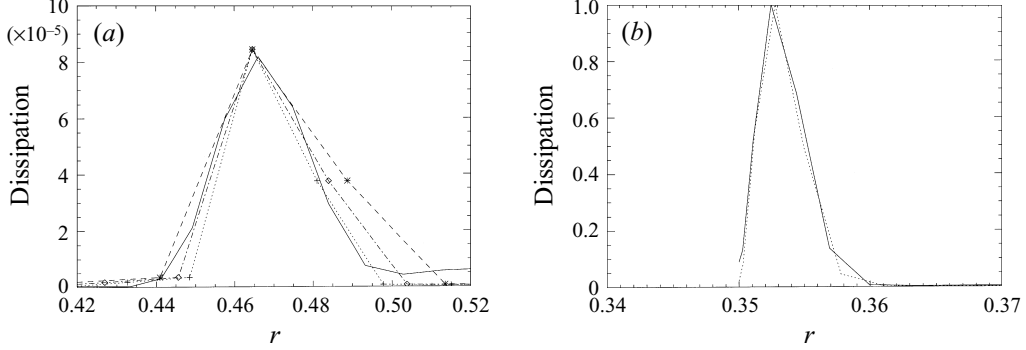
FIGURE 12. (*a*) Profiles of the dissipation rate across the shear layer spawned by the singularity at critical latitude for the spin-over mode. The solid line is for $E = 10^{-6}$ and other lines for $E = 10^{-8}$. The horizontal scale for the $E = 10^{-8}$-curves has been magnified by a factor $100^{1/4}$ for the dotted line, $100^{1/3}$ for the dashed line and $100^{2/7}$ for the dashed-dotted line. (*b*) Profiles of the dissipation rate in the radial direction at critical latitude. The solid line is for $E = 4 \times 10^{-7}$, the dashed line for $E = 10^{-8}$. The horizontal scale for the $E = 10^{-8}$ curve has been magnified by the factor $(4 \times 10^{-7}/10^{-8})^{2/5}$.

Kerswell 1995) do not show up very clearly in dissipation plots. Like Hollerbach & Kerswell (1995), we computed the spin-over mode (2,1,1) and investigated the scaling of the shear layer emitted by the singularity of the boundary layer on the inner sphere. As shown by figure 12(*a*), a width scaling with $E^{1/3}$ is not apparent; rather a scaling with $E^{1/4}$ or $E^{2/7}$ fits better. This suggests that the structure of such layers is similar to the structure of vertical layers in steady flows (see Stewartson 1966). Hence, discontinuities in azimuthal velocity would be smoothed out by $E^{1/4}$- and $E^{2/7}$-layers while $E^{1/3}$-layers would accommodate discontinuities in the second derivative.

The last case corresponds to the shear layer of width $O(E^{2/5})$ surrounding the critical latitude on the inner bounding sphere (see figure 12*b*). The scaling exponent 2/5 is rather clear.

These observations show that a large variety of scalings exists in the structure of inertial modes. In most cases the width of rays is either independent of E or scales with $E^{1/4}$. $E^{1/3}$-layers are not conspicuous and seem to play a hidden role, probably related to the smoothing of the second derivative of the azimuthal velocity as in vertical shear layers (Stewartson 1966).

3.4. *Trapped modes*

We shall now dwell a little on equatorially trapped modes. Such modes have been much investigated in the past in the search for solutions to the inviscid problem (see Israeli 1972; Stewartson 1971, 1972*a*, *b*).

Research on trapped modes has been essentially based on the study of characteristics propagation and identification of conditions where closed trajectories exist. However Israeli made a first attempt to find these modes in a real situation, i.e. computing numerically axisymmetric inertial modes excited through a periodic modulation of the rotational frequency.

His results did indeed reveal modes in which kinetic energy was concentrated near the equator. These modes were presented as belonging to a family of closed ray

(a)

$\omega = 3.19 \quad \tau = -4.06 \times 10^{-2}$

(b)
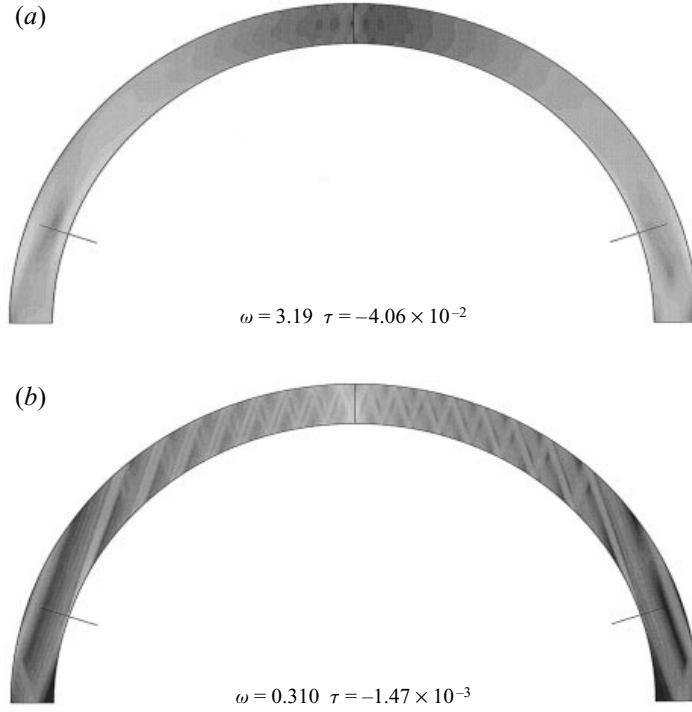

$\omega = 0.310 \quad \tau = -1.47 \times 10^{-3}$

FIGURE 13. Trapped mode found by Israeli (1972) with $E = 1.389 \times 10^{-5}$ (a) and the corresponding mode when $E = 8 \times 10^{-8}$ (b).

patterns with one loop near the equator and a frequency in the interval

$$\omega_l \leqslant \omega \leqslant \omega_u \tag{3.2}$$

with $\omega_l = (4 - \eta^2 - \eta(8 + \eta^2)^{1/2})/8$ and ω_u being solution of the following algebraic equation†:

$$\frac{(2 - 5\omega^2 + 4\omega^4)^2}{(1 - \omega^2)(1 - 2\omega^2)^2} + \frac{\omega^2(3 - 4\omega^2)^2}{(1 - 2\omega^2)^2} = \frac{4}{\eta^2}.$$

Using the same thin shell ($\eta = 0.875$) and the same Ekman number ($E = 1.389 \times 10^{-5}$) as Israeli, we indeed found a mode which looks trapped near the equator (see figure 13a). As this Ekman number is quite large however, and since the derivation of (3.2) is supposed to apply to the inviscid problem, we investigated the behaviour of this mode as the Ekman number is decreased. Quite surprisingly the trapping disappeared altogether as illustrated by figure 13b. The path of the eigenvalue in the complex plane is shown in figure 14.

For $\eta = 0.875$ the interval (3.2) is

$$0.283677 \leqslant \omega \leqslant 0.321392.$$

We scanned this whole band using an Ekman number of 8×10^{-8} and we did not find any trapped modes among the least-damped modes. There remains a possibility that such modes are strongly damped and hence difficult to find. Up to now, we have

† Note that Israeli's equation (6.1) is different from ours; likely this is a misprint as his asymptotic expression for $\omega \to 0$ is compatible with our equation but not with his own one.
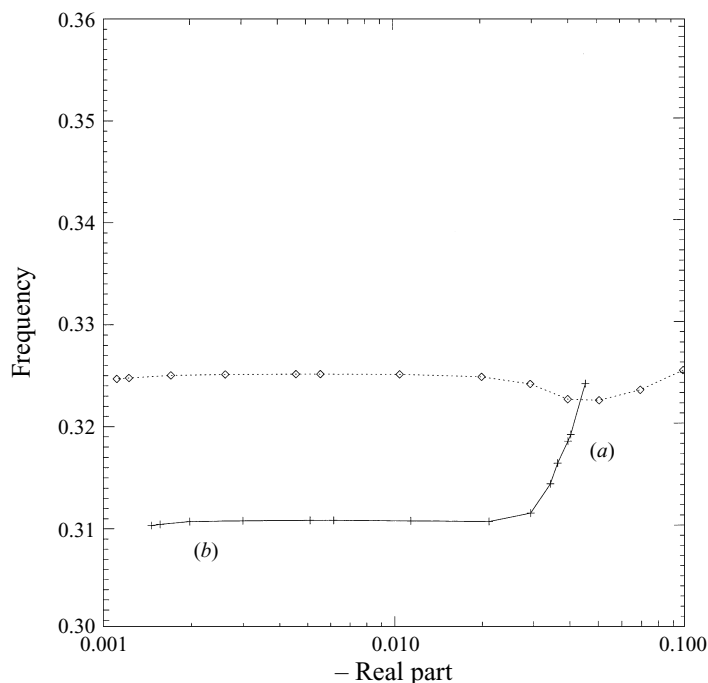
FIGURE 14. Path in the complex plane of the trapped mode found by Israeli (1972) for the $\eta = 0.875$ shell (solid line). The dotted line traces the path of a neighbouring eigenvalue. Both curves start at $E = 2 \times 10^{-5}$ and end at $E = 8 \times 10^{-8}$. On the descending branch near (*a*) the kinetic energy of the mode is trapped near the equator as on figure 13(*a*), while on the horizontal branch (*b*) the mode fills the whole shell as on figure 13(*b*).

found trapped modes only in cases with large viscosity. As illustrated by figure 15, equatorial or polar trapping is easily found for a thin shell with $E = 10^{-3}$.

These results suggest that the trapping presented here and also found by Israeli is strongly influenced by viscosity and may not be related to the trapping deduced from ray patterns. They also support the doubts raised by Stewartson (1972*b*) about the very existence of trapped modes for slightly viscous fluids.
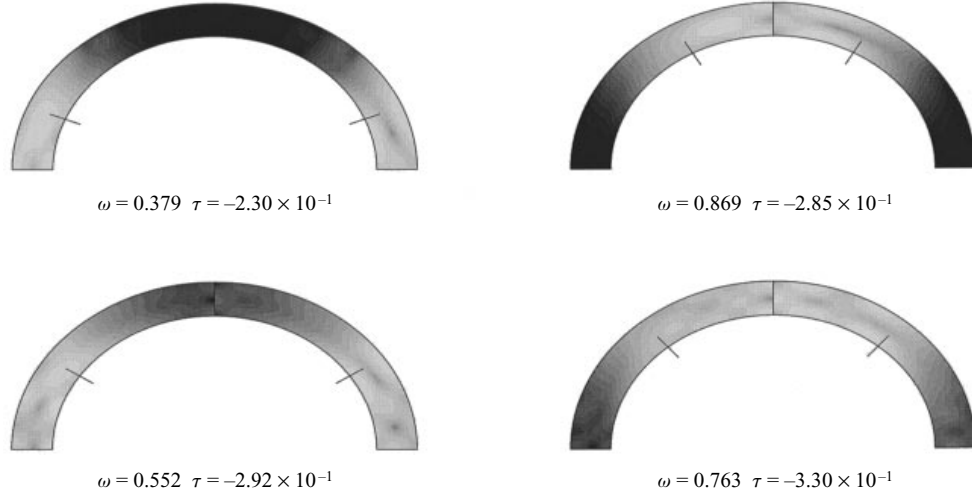
3.5. *Spectra*

To end this section we now turn to the spectral properties of the modes and investigate how eigenvalues are distributed in the complex plane and how they evolve with the Ekman number.

It has already been noticed (see §3.1) that the paths of eigenvalues may cross in the complex plane. In this particular case, crossing happens because one of the eigenvalues has a real part which decreases more slowly than the other (see table 1).

If we now consider the behaviour of the eigenvalue of the thin-shell mode (with $\omega \sim 0.743$), it is also non-monotonic due to the pattern changes. When the pattern remains the same, the damping rate is proportional to E, but when the bifurcation occurs in the interval $10^{-9} \lesssim E \lesssim 10^{-8}$ the damping rate is almost constant (table 2).

The preceding results show that no simple rule governs the decrease of the damping rate of a particular eigenvalue when viscosity diminishes. However, this is not the case when the whole spectrum (set) of eigenvalues is considered. In figures 16(*a*) and 17(*a*) we have plotted all the eigenvalues for different Ekman numbers and $\eta = 0.35$. The

$\omega = 0.379 \quad \tau = -2.30 \times 10^{-1}$

$\omega = 0.869 \quad \tau = -2.85 \times 10^{-1}$

$\omega = 0.552 \quad \tau = -2.92 \times 10^{-1}$

$\omega = 0.763 \quad \tau = -3.30 \times 10^{-1}$

FIGURE 15. Modes trapped near the pole or the equator for the $\eta = 0.8$ shell with $E = 10^{-3}$.

E	$|\text{Im}(\lambda(\text{I}_{\eta=0.35}))|$	$|\text{Re}(\lambda(\text{I}_{\eta=0.35}))|/E^{0.5}$	$|\text{Im}(\lambda(\text{II}_{\eta=0.35}))|$	$|\text{Re}(\lambda(\text{II}_{\eta=0.35}))|/E^{0.93}$
1.0×10^{-8}	0.6598	2.94	0.66291	741
5.0×10^{-8}	0.6599	3.01	0.66290	683
1.0×10^{-7}	0.6599	2.96	0.66289	668
2.0×10^{-7}	0.6600	3.00	0.66288	659
4.0×10^{-7}	0.6602	2.99	0.66280	667
6.0×10^{-7}	0.6603	3.11	0.66266	669
8.0×10^{-7}	0.6605	3.28	0.66242	665
9.0×10^{-7}	0.6607	3.38	0.66226	658
1.0×10^{-6}	0.6609	3.55	0.66203	639

TABLE 1. Variation of the eigenvalues of figure 3 with the Ekman number for $\eta = 0.35$.

E	$|\text{Im}(\lambda)|$	$|\text{Re}(\lambda)|$	$|\text{Re}(\lambda)|/E$
$1. \times 10^{-9}$	0.74295	2.18×10^{-5}	21821
$1. \times 10^{-8}$	0.74299	2.29×10^{-5}	2293
$1. \times 10^{-7}$	0.74299	8.07×10^{-5}	806
$1. \times 10^{-6}$	0.74300	7.58×10^{-4}	758
$2. \times 10^{-6}$	0.74299	1.49×10^{-3}	747
$4. \times 10^{-6}$	0.74301	2.93×10^{-3}	732
$1. \times 10^{-5}$	0.74305	7.03×10^{-3}	703

TABLE 2. Variation of the eigenvalue of the thin shell ($\omega \sim 0.743$) with the Ekman number. Note the bifurcation at $E = 10^{-8}$.

remarkable fact is that the distribution of eigenvalues remains the same statistically when the real parts are scaled by $E^{2/3}$. This behaviour is quite surprising if we remember the results on shear layers presented in §3.3. If shear layers are indeed of width $O(E^{1/4})$ and if they do not fill the fluid's volume, then the damping rate should scale with $E^{1/2}$. Such a case, exemplified by the mode displayed on figure 6(*a*), is therefore not commonplace. The scaling in $E^{2/3}$ of the damping rate of modes in
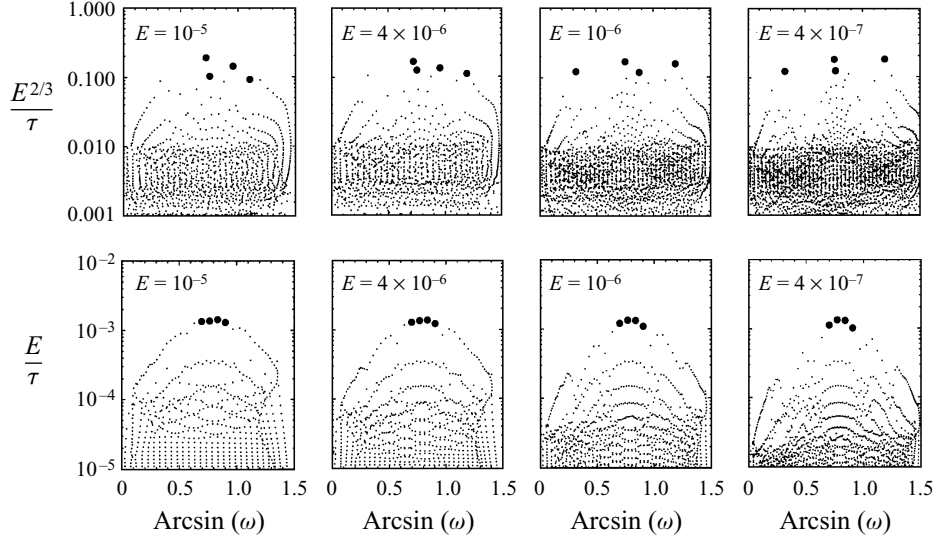
FIGURE 16. Distribution of eigenvalues in the complex plane for different values of the Ekman number. The top and bottom rows are respectively for the thick and thin shells ($\eta = 0.35$ and $\eta = 0.80$). For each eigenvalue the inverse of the damping rates ($\tau = |\mathrm{Re}(\lambda)|$) multiplied by the $E^{2/3}$ is plotted as a function of the associated critical latitude. The circles emphasize the four least-damped modes. Note the important changes among these modes for $\eta = 0.35$ as the Ekman number is decreased.
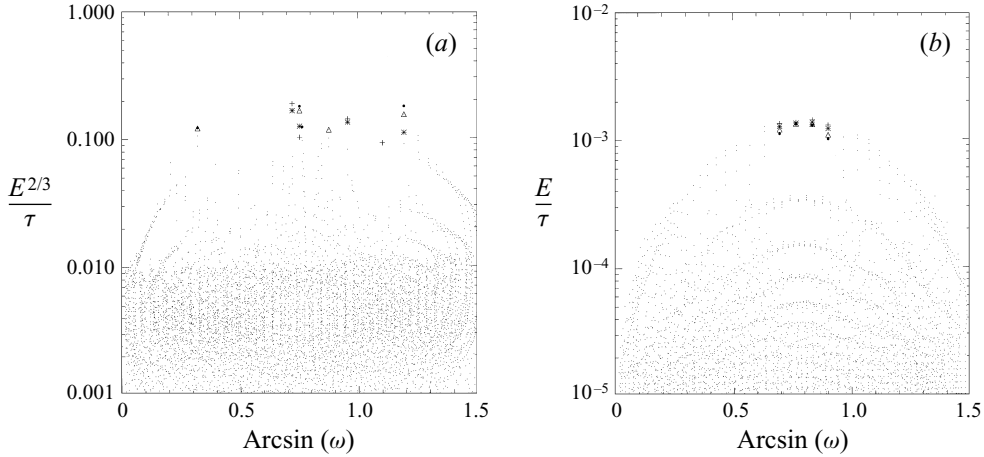

FIGURE 17. Superposition of the four plots of figure 16 for the two shells: (a) $\eta = 0.35$, (b) $\eta = 0.80$. The four least-damped modes are now shown as: $+$, $E = 10^{-5}$; $*$, $E = 4 \times 10^{-6}$; $\triangle$, $E = 10^{-6}$; $\bullet$, $E = 4 \times 10^{-7}$.

the thick shell may be understood if we consider that the smallest scales which may be found far from the boundaries are $O(E^{1/3})$. Wood (1966) has shown that velocity gradients then scale with $E^{-1/6}$. If the web of rays is space-filling then dissipation is $O(E^{2/3})$. A typical example of such a mode is the one displayed on figure 6(b). The scaling in $E^{1/4}$ would appear only for isolated shear layers. Statically, modes with a space-filling web are more numerous and therefore eigenvalues with $O(E^{2/3})$ real parts dominate the spectrum. Moreover, eigenvalues may each evolve in their own way
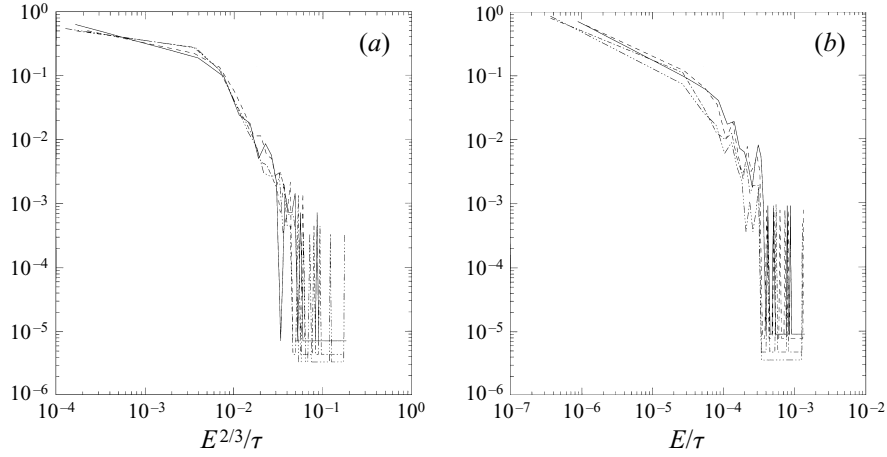
FIGURE 18. Histograms for the different plots of figure 16 for the two shells. These histograms show the density of real parts of eigenvalues. These quantities are scaled in the same way as on figure 17. The four types of lines are for the four different Ekman numbers.

when viscosity is changed and do not converge to any precise value in the inviscid limit, but their distribution, having invariant scaling properties like a mean damping rate scaling with $E^{2/3}$, would remain the same. Figure 18 illustrates in another way the scaling of the distribution of real parts.

We have examined the case of the thin shell and quite surprisingly the exponent was closer to unity, as shown by figures 16(*b*) and 17(*b*). The reason may simply be that for the cases considered the Ekman number is still too large (scaling the Ekman number with the thickness of the shell as the length-scale makes the Ekman number ten times larger for the thin shell than for the thick shell), not many bifurcations have taken place and the asymptotic regime has not yet been reached. However, note the progressive disappearance of families of eigenvalues (lines in the complex plane) as the Ekman number is reduced and the rise of chaos in the distribution of eigenvalues.

4. Conclusions

We have presented in this paper numerical computations of inertial modes in a spherical shell. Using an iterative procedure based on the incomplete Arnoldi–Chebyshev method, we have been able to compute these modes for very small Ekman numbers.

The first result of these calculations is that inertial modes in a spherical shell are strongly featured by a web of rays which reflect at the boundaries. Kinetic energy is not evenly distributed in the volume of the shell but concentrated on conical surfaces which have some thickness however. The intersection of these 'surfaces' with a meridional section forms the web of rays. The thickness of rays has been observed to be either independent of viscosity or scaling with $E^{1/4}$ while spatial frequencies $O(E^{-1/3})$ are needed to explain the statistical behaviour of real parts of eigenvalues. These observations require a detailed analysis of time-dependent shear layers in order to complete the work of Gans (1983) who found $E^{1/4}$ and $E^{1/3}$ scalings for these layers. Quite probably, such an analysis would reveal nested boundary layers just as in the case of steady vertical shear layers.

We have also shown that the web of rays depends on viscosity. We have given an example of a mode where the pattern of rays bifurcates as the viscosity is decreased. During this bifurcation, the modal frequency remains almost the same while the damping rate increases considerably because of the small-scale features which arise. Such bifurcations may occur again and again as the viscosity is decreased and we have given arguments in favour of such a scenario. Then one should expect that no asymptotic smooth solution exists (except for the case described in Appendix B); but we cannot exclude the possibility of fractal solutions. We have also shown that instead of looking for asymptotic solutions for each eigenmode, one should concentrate on the statistical properties of eigenvalues.

In fact, the present problem has connections with quantum chaos. Indeed, quantum chaos appears for semi-classical systems when the wave function and its associated eigenvalue (the energy) depend sensitively on a control parameter of the system. Energy levels may then evolve in a chaotic way as the control parameter is changed. However, the statistics of energy levels (or rather the difference between energy levels) obeys some simple rules which have been much studied in recent years (Nakamura 1993). One may note that our operators, unlike Hamiltonians in quantum mechanics, are not Hermitian and eigenvalues are not real (unlike energy). Still, the analogy with quantum mechanics remains for quantum chaos has also been observed in systems (of nuclear physics) with finite-lifetime states. For such systems, the analogy with fluid mechanics is very strong: the frequency of a mode is related to its 'quantum-energy' while the damping rate is nothing but the inverse of its lifetime. We shall not develop this analogy further here as it will be the subject of a forthcoming paper.

Another side of the question about the inviscid limit may however be studied with the rays orbits as recently done by Maas & Lam (1995) for internal gravity modes in a basin. These authors have been able to construct analytical solutions to their inviscid problem. However, these solutions are infinitely degenerate and only the inclusion of viscosity can help in selecting the right eigenvector. Inertial modes share great similarities with gravity modes and likely solutions to the inviscid problem can be constructed using characteristics propagation. However, one will also face the infinite degeneracy of the eigenvalues and the problem of predicting the shape of the least-damped modes for small but finite viscosity will remain. Using inviscid solutions may also be misleading: the case of trapped modes has shown that this problem has also its own traps!

Finally let us come back to astrophysics and geophysics. A standard problem is the detection of the modes, their identification and their use to constrain models. Modes most easily detected are generally large-scale ones and therefore the most interesting part of the spectrum is that close to the imaginary axis. Modes like those of Appendix B will emerge naturally as their eigenfunction is very smooth. However the structure of other modes depends crucially on the viscosity. Hence the emergence of one of these modes may yield a direct estimation of the fluid's viscosity. This supposes however that one is able to compute modes at very small Ekman numbers (for astrophysical or geophysical cases, it is usually less than 10^{-10}) since extrapolation from higher values is hazardous because of the chaos arising in the distribution of eigenvalues.

Appendix A

In this Appendix we shall prove that in a thin ray propagating towards the polar axis, the kinetic energy is proportional to the inverse of the distance to the axis.

We consider the linearized inviscid equations

$$i\omega \boldsymbol{v} + \boldsymbol{e}_z \times \boldsymbol{v} = -\nabla p,$$

$$\nabla \cdot \boldsymbol{v} = 0.$$

In cylindrical coordinates (s, ϑ, z) they take the form

$$i\omega v_s - v_\vartheta = -\frac{\partial p}{\partial s} \quad i\omega v_\vartheta + v_s = 0,$$

$$i\omega v_z = -\frac{\partial p}{\partial z}, \quad \frac{1}{s}\frac{\partial}{\partial s}(sv_s) + \frac{\partial v_z}{\partial z} = 0.$$

Eliminating the velocity from these equations we get Poincaré equation for the pressure

$$\frac{\omega^2}{1-\omega^2}\frac{\partial^2 p}{\partial s^2} + \frac{\omega^2}{1-\omega^2}\frac{1}{s}\frac{\partial p}{\partial s} - \frac{\partial^2 p}{\partial z^2} = 0. \tag{A 1}$$

Let us define

$$\alpha \equiv \omega, \quad \beta \equiv (1-\omega^2)^{1/2}, \quad \alpha^2 + \beta^2 = 1.$$

We make the following change of variables:

$$u = \alpha s - \beta z, \quad v = \beta s + \alpha z.$$

We have then

$$s = \alpha u + \beta v, \quad z = -\beta u + \alpha v.$$

The equation for the pressure (A 1) becomes

$$\frac{\alpha^4 - \beta^4}{\beta^2}\frac{\partial^2 p}{\partial u^2} + \frac{2\alpha}{\beta}\frac{\partial^2 p}{\partial u\partial v} + \frac{\alpha^2}{\beta^2}\frac{1}{\alpha u + \beta v}\left(\alpha\frac{\partial p}{\partial u} + \beta\frac{\partial p}{\partial v}\right) = 0. \tag{A 2}$$

We now make the fundamental hypothesis that the variation along the ray propagation direction is much smaller than the variation across the ray, that is that the rays are very thin:

$$\frac{\partial}{\partial v} \gg \frac{\partial}{\partial u}.$$

Defining the new variable $\psi \equiv \partial p/\partial v$, equation (A 2) becomes

$$2(\alpha u + \beta v)\frac{\partial \psi}{\partial u} + \alpha\psi = 0, \quad \frac{\partial \log \psi}{\partial u} = -\frac{\alpha}{2(\alpha u + \beta v)},$$

$$\psi = g(v)(\alpha u + \beta v)^{-1/2},$$

with $g(v)$ some (positive) function of v.

Under the hypothesis $\partial/\partial v \gg \partial/\partial u$ the velocity components are given by

$$v_s \simeq -\frac{i\omega}{1-\omega^2}\beta\psi = -\frac{i\omega}{(1-\omega^2)^{1/2}}\frac{g(v)}{s^{1/2}},$$

$$v_\vartheta = -\frac{v_s}{i\omega} \simeq \frac{1}{(1-\omega^2)^{1/2}}\frac{g(v)}{s^{1/2}},$$

$$v_z = -\frac{1}{i\omega}\frac{\partial p}{\partial z} \simeq \frac{ig(v)}{s^{1/2}}.$$

From this we see that when $s \to 0$ along the rays the velocity components diverge like $s^{-1/2}$ and the kinetic energy grows like $s^{1/2}$. This also shows that the flux of momentum is conserved along the rays.

Now if $\boldsymbol{e}_v$ denotes the direction perpendicular to the rays, we have $\boldsymbol{e}_v = \beta\boldsymbol{e}_s + \alpha\boldsymbol{e}_z$ and therefore $\boldsymbol{v} \cdot \boldsymbol{e}_v = 0$ on the rays. The velocity is thus parallel to the ray as shown by figure 7. This result which shows that meridional velocity of axisymmetric modes is always parallel to characteristics, may be obtained more directly from the inviscid equations of motion. As

$$v_s = -\frac{i\omega}{1-\omega^2}\frac{\partial p}{\partial s}, \qquad v_z = \frac{i}{\omega}\frac{\partial p}{\partial z}$$

we find that

$$\boldsymbol{v} \cdot \boldsymbol{\nabla} p = \frac{i}{\omega}\left(\frac{\partial p}{\partial z} - \frac{\omega}{(1-\omega^2)^{1/2}}\frac{\partial p}{\partial r}\right)\left(\frac{\partial p}{\partial z} + \frac{\omega}{(1-\omega^2)^{1/2}}\frac{\partial p}{\partial r}\right).$$

On characteristics which are also isobars, the right-hand side is always zero. The meridional velocity is therefore parallel to the rays.

Appendix B

There exist analytical solutions of the system (2.2) when $E = 0$, in the form of purely toroidal modes. These are

$$w_m^m(r) = Ar^m \qquad \lambda = i\omega_n = \frac{i}{m+1}$$

with all other radial functions set to zero. The associated velocity field is

$$v_\theta = Ar^m(\sin\theta)^{m-1}\sin(m\phi + \omega_m t),$$

$$v_\phi = Ar^m(\sin\theta)^{m-1}\cos\theta\cos(m\phi + \omega_m t).$$

For $m = 1$ one recovers the spin-over mode.

REFERENCES

ALDRIDGE, K. D. & LUMB, L. 1987 Inertial waves identified in the Earth's fluid outer core. *Nature* **325**, 421–423.

BRACONNIER, T., CHATELIN, F. & DUNYACH, J.-C. 1995 Highly nonnormal eigenvalue problems in the aeronautical industry. *Japan J. Ind. Appl. Maths* **12**, 123–136.

BRYAN, G. 1889 The waves on a rotating liquid spheroid of finite ellipticity. *Phil. Trans. R. Soc. Lond.* **180**, 187–219.

CHOSSAT, P. 1979 Bifurcation and stability of convective flows in a rotating or not rotating spherical shell. *SIAM J. Appl. Maths* **37**, 624–647.

FOX, L. & PARKER, I. 1968 *Chebyshev Polynomials in Numerical Analysis.* Oxford University Press.

GANS, R. 1983 Boundary layers on characteristic surfaces for time-dependent rotating flows. *Trans. ASME: J. Appl. Mech.* **50**, 251.

GARDNER, D. R., TROGDON, S. A. & DOUGLAS, R. W. 1989 A modified tau spectral method that eliminates spurious eigenvalues. *J. Comput. Phys.* **80**, 137–167.

GOTTLIEB, D. & ORSZAG, S. A. 1977 *Numerical Analysis of Spectral Methods: Theory and Applications.* SIAM-CBMS, Philadelphia.

GREENSPAN, H. P. 1969 *The Theory of Rotating Fluids.* Cambridge University Press.

HOLLERBACH, R. & KERSWELL, R. 1995 Oscillatory internal shear layers in rotating and precessing flows. *J. Fluid Mech.* **298**, 327–339.

ISRAELI, M. 1972 On trapped modes of rotating fluids in spherical shells. *Stud. Appl. Maths* **51**, 219–237.

KERSWELL, R. 1994 Tidal excitation of hydromagnetic waves and their damping in the Earth. *J. Fluid Mech.* **274**, 219–241.

KERSWELL, R. 1995 On the internal shear layers spawned by the critical regions in oscillatory Ekman boundary layers. *J. Fluid Mech.* **298**, 311–325.

LUMB, L. & ALDRIDGE, K. D. 1991 On viscosity estimates for the Earth's fluid outer core and core-mantle coupling. *J. Geomag. Geoelectr.* **43**, 93–110.

LUMB, L., ALDRIDGE, K. D. & HENDERSON, G. 1993 A generalized 'core resonance' phenomenon: Inferences from a Poincaré core model. In *Dynamics of Earth's Deep Interior and Earth Rotation* (ed. J. L. Le Mouël, D. Smylie & T. Herring), p. 51. IUGG.

MAAS, L. & LAM, F.-P. 1995 Geometric focusing of internal waves. *J. Fluid Mech.* **300**, 1–41.

McFADDEN, G. B., MURRAY, B. T. & BOISVERT, R. F. 1990 Elimination of spurious eigenvalues in the chebyshev tau spectral method. *J. Comput. Phys.* **91**, 228–239.

NAKAMURA, K. 1993 *Quantum Chaos – a New Paradigm of Nonlinear Dynamics.* Cambridge University Press.

NEUBERG, J., HINDERER, J. & ZÜRN, W. 1987 Stacking gravity tide observations in central europe for the retrieval of the complex eigenfrequency of the nearly diurnal free-wobble. *Geophys. J. R. Astron. Soc.* **91**, 853–868.

ORSZAG, S. A. 1971 Accurate solution of the Orr-Sommerfeld stability equation. *J. Fluid Mech.* **50**, 689–703.

RIEUTORD, M. 1987 Linear theory of rotating fluids using spherical harmonics. I. Steady flows. *Geophys. Astrophys. Fluid Dyn.* **39**, 163.

RIEUTORD, M. 1991 Linear theory of rotating fluids using spherical harmonics. II. Time periodic flows. *Geophys. Astrophys. Fluid Dyn.* **59**, 185–208.

RIEUTORD, M. 1995 Inertial modes in the liquid core of the Earth. *Phys. Earth Plan. Intl* **91**, 41–46.

ROBERTS, P. H. 1988 Future of geodynamo theory. *Geophys. Astrophys. Fluid Dyn.* **44**, 3–31.

STEWARTSON, K. 1957 On almost rigid rotations. *J. Fluid Mech.* **3**, 17–26.

STEWARTSON, K. 1966 On almost rigid rotations. Part 2. *J. Fluid Mech.* **26**, 131–144.

STEWARTSON, K. 1971 On trapped oscillations of a rotating fluid in a thin spherical shell. *Tellus* **23**, 506–510.

STEWARTSON, K. 1972a On trapped oscillations of a rotating fluid in a thin spherical shell II. *Tellus* **24**, 283–287.

STEWARTSON, K. 1972b On trapped oscillations in a slightly viscous rotating fluid. *J. Fluid Mech.* **54**, 749–761.

STEWARTSON, K. & RICKARD, J. 1969 Pathological oscillations of a rotating fluid. *J. Fluid Mech.* **35**, 759–773.

WALTON, I. 1975 Viscous shear layers in an oscillating rotating fluid. *Proc. R. Soc. Lond.* A **344**, 101–110.

WOOD, W. 1966 An oscillatory disturbance of rigidly rotating fluid. *Proc. R. Soc. Lond.* A **293**, 181–212.